A CATALOG OF MID-INFRARED SOURCES IN THE EXTENDED GROTH STRIP

P. BARMBY,[1,2] J.-S. HUANG,[1] M. L. N. ASHBY,[1] P. R. M. EISENHARDT,[3]
G. G. FAZIO,[1] S. P. WILLNER,[1] AND E. L. WRIGHT[4]

ABSTRACT

The Extended Groth Strip (EGS) is one of the premier fields for extragalactic deep surveys. Deep observations of the EGS with the Infrared Array Camera (IRAC) on the *Spitzer Space Telescope* cover an area of $0.38 \deg^2$ to a 50% completeness limit of 1.5 μJy at 3.6 μm. The catalog comprises 57,434 objects detected at 3.6 μm, with 84%, 28%, and 24% also detected at 4.5, 5.8, and 8.0 μm, respectively. Number counts are consistent with results from other *Spitzer* surveys. Color distributions show that the EGS IRAC sources comprise a mixture of populations: low-redshift star-forming galaxies, quiescent galaxies dominated by stellar emission at a range of redshifts, and high-redshift galaxies and AGNs.

Subject headings: catalogs — galaxies: high-redshift — infrared: galaxies — surveys

Online material: machine-readable table

1. INTRODUCTION

Observations of unbiased, flux-limited galaxy samples via "blank-field" extragalactic surveys have been a mainstay in the field of galaxy formation and evolution for several decades, with the well-known Hubble Deep Field (Williams et al. 1996) and Sloan Digital Sky Survey (York et al. 2000) exemplifying two very different types of galaxy survey. Extending the wavelength coverage as broadly as possible has led to numerous changes in the understanding of how galaxies form, evolve, and interact over cosmic time. New technologies and larger telescopes continually increase the volume of discovery space, making some "state-of-the-art" observations obsolete in just a few years.

The locations of extragalactic survey fields are driven by a number of considerations. To achieve the deepest possible data, foreground diffuse emission and absorption should be low. Relevant properties include Galactic H I column density (particularly important for X-ray observations), Galactic and ecliptic dust and "cirrus" foreground emission (particularly important for infrared observations), schedulability (for observability by space-based telescopes), and a lack of extremely bright foreground sources such as stars or nearby galaxies. There is of course a trade off between ecliptic latitude and declination; high-latitude fields are less easily observable from both hemispheres. The Extended Groth Strip (EGS), centered at $\alpha = 14^{\rm h}17^{\rm m}$, $\delta = +52°30'$, is observable only from the north, but has excellent properties in other categories and as such is one of a handful of premier extragalactic survey fields. Observations of the EGS have now been made at nearly every wavelength, with a number of projects (including the *Spitzer* Legacy project FIDEL) still ongoing. Many of the data sets in the EGS region are described briefly by Davis et al. (2007); the same journal issue contains the results of initial studies using the multiwavelength data set. As part of a public data release by the AEGIS collaboration, this paper describes observations of the EGS made with the Infrared Array Camera (IRAC; Fazio et al. 2004b) on the *Spitzer Space Telescope* (Werner et al. 2004) and presents a catalog derived from those data.

IRAC is sensitive to radiation nearly out of reach for ground-based telescopes. It was designed in part to study galaxies at high redshift; its four bands at 3.6, 4.5, 5.8, and 8.0 μm probe the peak of the galaxy spectral energy distribution out to redshifts of $z = 4$. Early results from the *Spitzer* mission (e.g., Barmby et al. 2004) established that IRAC could indeed detect $z = 3$ galaxies, and lensed sources at much higher redshifts ($z \sim 7$) have also been detected (Egami et al. 2005). The population of galaxies detected with the MIPS instrument on *Spitzer* (Rieke et al. 2004) have been well-characterized (Pérez-González et al. 2005; Le Floc'h et al. 2005), as have the IRAC sources detected in shallow surveys such as SWIRE (Rowan-Robinson et al. 2005) and the Bootes field (Eisenhardt et al. 2004). However, the IRAC sources detected in deep observations such as those made of the EGS (90 times the exposure time of SWIRE) or the GOODS fields (1500 times the exposure time) have only begun to be explored (e.g., Pérez-González et al. 2008). This paper presents the IRAC EGS catalog and an examination of the source population; a companion paper (J.-S. Huang et al. 2008, in preparation) describes the use of the IRAC data in combination with optical data to derive photometric redshifts. Other recent papers by the IRAC team have used the EGS data to derive number counts (Fazio et al. 2004a), define a class of infrared luminous Lyman-break galaxies (Huang et al. 2005), explore the mid-infrared properties of X-ray sources (Barmby et al. 2006), identify mid-infrared counterparts to sub-millimeter sources (Ashby et al. 2006), investigate the contribution of mid-infrared sources to the submillimeter background (Dye et al. 2006), measure stellar masses for $z \sim 3$ Lyman-break galaxies (Rigopoulou et al. 2006), and identify 6 cm radio sources (Willner et al. 2006).

2. OBSERVATIONS AND DATA REDUCTION

The IRAC instrument was described by Fazio et al. (2004b) and Reach et al. (2006). The IRAC observations of the EGS were carried out as part of *Spitzer* Guaranteed Time Observing program number 8, using about 165 hr of time contributed by *Spitzer* Science Working Group members G. Fazio, G. Rieke, and E. Wright. The observations were performed in two epochs, 2003 December

[1] Harvard-Smithsonian Center for Astrophysics, 60 Garden Street, Cambridge, MA 02138.
[2] Current address: Department of Physics and Astronomy, University of Western Ontario, London, ON N6A 3K7, Canada; pbarmby@uwo.ca.
[3] Jet Propulsion Laboratory, California Institute of Technology, Pasadena, CA 91109.
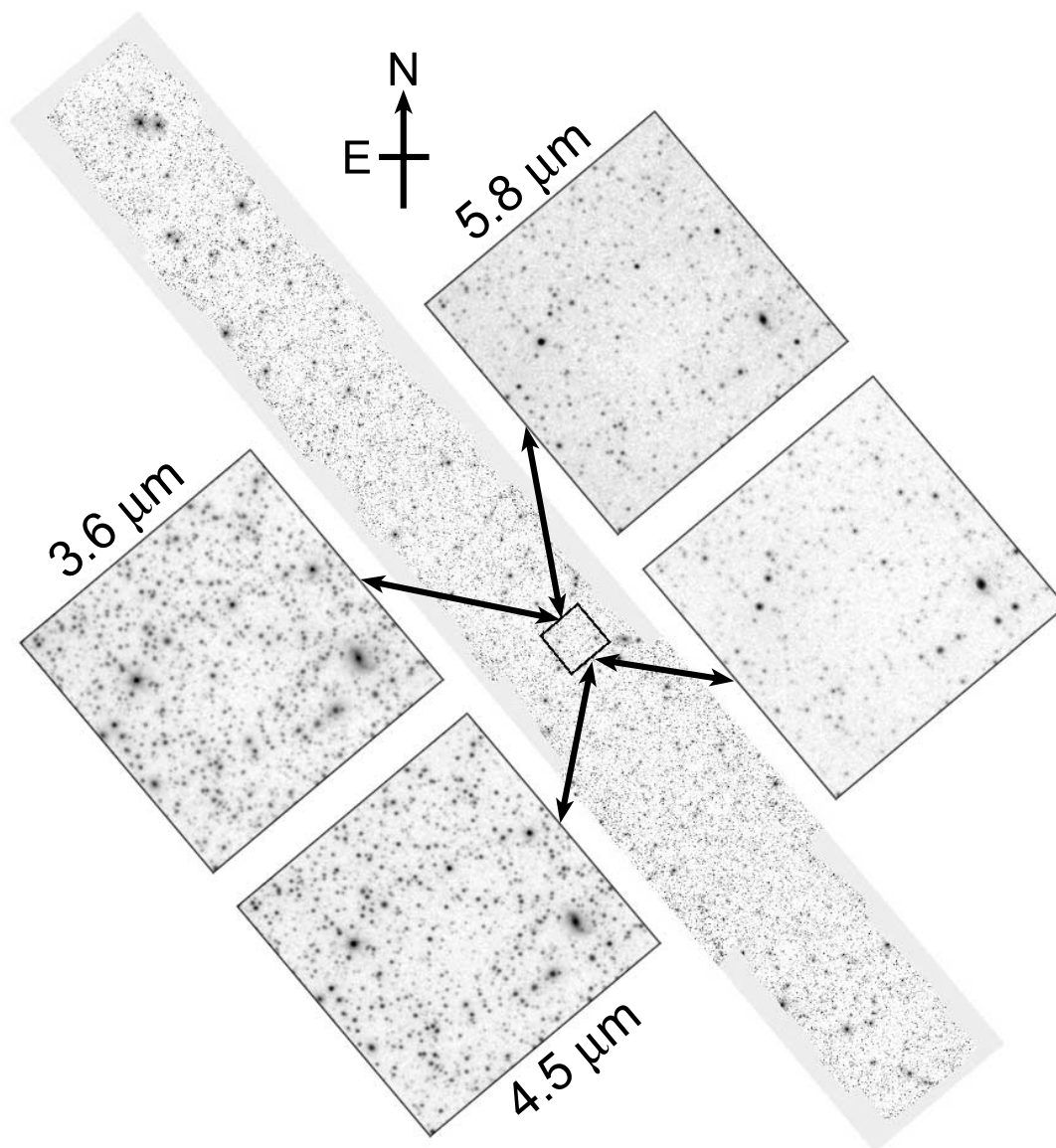[4] UCLA Astronomy, P.O. Box 951547, Los Angeles, CA 90095-1547.

Fig. 1.—Extended Groth Strip as seen by IRAC (*negative image*). The long image is the full $2.3° \times 17.3'$ 3.6 μm mosaic shown with north up and east to the left. Insets show $5' \times 5'$ cutouts in each of the four bands; the 3.6 and 4.5 μm images have much higher source density than the 5.8 and 8.0 μm images. The 7.8 arcmin^2 region masked due to artifacts is between the two bright stars at the northeast end of the strip.

and 2004 June/July. (Source variability between the two epochs is under analysis and will be discussed in a future contribution.) Each epoch's observations consisted of 26 Astronomical Observing Requests (AORs) with each AOR implemented as a 2 column (across the width of the strip) by 1 row map having 26 dithered 200 s exposures[5] per map position. The dither pattern used was the medium-scale cycling pattern, which has a median separation of 53 pixels (64.7″) and includes half-pixel offsets. The central positions of the maps were defined to align with the EGS position angle, 40° east of north. Since the *Spitzer* roll-angle is not selectable by the observer, the correct orientation of the IRAC arrays (aligned with the EGS) was accomplished by constraining the observation dates. Each epoch's AORs were observed in order from south to north along the EGS to minimize roll angle changes between adjacent AORs and prevent gaps. Because the array position angles changed by 180° between the two epochs, and be-

cause IRAC has two separate fields of view offset by 5′, there are regions at the ends of the EGS with only single-epoch coverage in one field of view. To summarize, the IRAC observations comprise 52 positions in a $2° \times 10'$ map, and at each position there are 52 dithered 200 s exposures at 3.6, 4.5, and 5.8 μm and 208 dithered 50 s exposures taken concurrently at 8.0 μm. The processed data set includes 18,924 Basic Calibrated Data (BCD) images: only four of the expected frames were lost to pipeline problems.

Data processing began with the BCD images produced by version 14 of the Spitzer Science Center IRAC pipeline. Individual frames were corrected for the "muxbleed" and "pulldown" artifacts near bright stars by fitting and subtracting a straight line (counts as a function of pixel number) to the affected pixels. This somewhat crude correction reduced pulldown to a level below the noise, but some muxbleed trails are still apparent in the output mosaics. The known variation in point-source calibration over the IRAC arrays' field of view (Reach et al. 2005) was not corrected for: doing so would have compromised outlier detection during mosaicking and resulted in nonflat backgrounds in the final

---

[5] Because of the higher background levels in the 8.0 μm IRAC band, each 200 s exposure is implemented as four 50 s exposures.
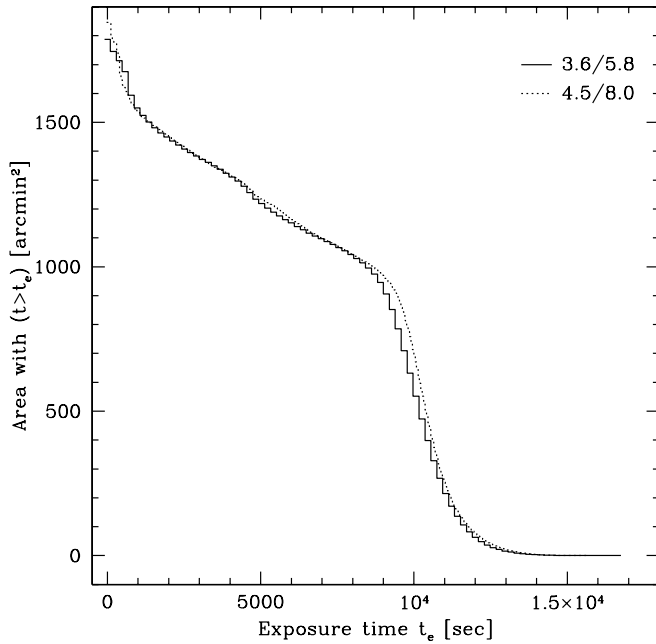
Fig. 2.—Cumulative area coverage as a function of exposure time for IRAC observations of the EGS. The median coverage is about 9100 s in all bands.

mosaics which would have greatly complicated source detection. Because the IRAC exposures are well dithered, the magnitude of this effect should be <1% (see the IRAC Data Handbook). IRAC photometry is known to vary slightly with source position within a pixel, but this effect is <2% and should also average out of the highly dithered EGS data. The saturation limits for the mosaics are the same as those in individual 200 s frames: 2 mJy ($m_{AB} = 15.7$) at 3.6 and 4.5 μm, and 14 mJy ($m_{AB} = 13.5$) at 5.8 and 8.0 μm.

Mosaicking was done using custom IDL scripts supplemented with procedures from the IDL Astronomy Library. A reference frame containing all the input frames in each band was constructed, and a grid of output pixels defined. The linear dimensions of the output pixels were half those of the input pixels. The individual input frames were distortion-corrected and projected onto the grid of output pixels using bilinear interpolation, then the pixel stack at each output pixel was combined by averaging with 3 $\sigma-$clipping. This σ-clipping served to reject cosmic rays, scattered light, and other image artifacts. Rejection of array row- and column-based artifacts was facilitated by having the observations done at two different position angles, but some artifacts remain in the final mosaics. The method used to remove these from the catalog is described in § 3. After mosaics in the four individual IRAC bands were constructed, they were transformed to a common pixel scale and reference frame using version 2.16.0

of the SWarp software written by E. Bertin, retrieved from the TERAPIX Web site. The final mosaics are $2.3° \times 0.29°$, with a pixel size (0.61″) about half the native IRAC pixel scale (1.22″). The mosaicking and resampling conserved surface brightness, so the mosaics, like the input BCD images, are in units of MJy sr^{-1}. Figure 1 shows a portion of the mosaics in each band. The mosaics, coverage images, and point-spread function (PSF) star images (see below) are available online.[6]

Because of dithering the coverage varies over the mosaics; the median coverage is about 47 frames (9100 s) in all channels. The number of frames co-added at each position was recorded during processing, and a cumulative plot of the exposure time per pixel is shown in Figure 2. Pixels with lower coverage depth are in the "crust" near the edges of the mosaic, and the small fraction of pixels with significantly higher coverage are located along the center line where different map positions overlap. Within the deep coverage area, the coverage differs slightly between the IRAC bands due to the differing fields of view and appearance of artifacts. (For example, cosmic ray hits affect more pixels in the 5.8 and 8.0 μm bands, but bright-source artifacts affect more pixels in the 3.6 and 4.5 μm bands.) The inflection points in the coverage curves are at areas/depths of 1440 arcmin^2/1900 s and 930 arcmin^2/9100 s. About 100 arcmin^2 is covered to depths of >11,500 s, but this deepest area is not contiguous.

Measuring the PSFs of the mosaics is important for quantifying the distribution of light within individual sources. A "PSF star image" was constructed in each band using the SSC `prf_estimate` software (ver. 030106) to combine "postage stamp" images of bright sources (ranging from 50 sources at 8.0 μm to 350 at 3.6 μm) in the mosaics. Although the PSF is known to vary over the IRAC field of view, this effect is smoothed over in mosaicking, and in any case, the variation was not important for our purposes. The medians and standard deviations of photometry offsets between small measurement apertures and the IRAC calibration photometry aperture of 12.2″ were computed over the ensembles of bright sources; these are given in Table 1. The aperture corrections derived here compare reasonably well with those found by other groups (e.g., Pérez-González et al. 2008; Papovich et al. 2006; Surace et al. 2005), particularly for the larger apertures where the uncertainties are smaller.

Computing photometric uncertainties requires a good understanding of image noise properties. Noise in the mosaics comes from several sources. The most fundamental is photon shot noise from the Zodiacal foreground, which for measurements in small beams is a factor of 30 smaller than the catalog limit at 3.6 and 4.5 μm and a factor of 10 smaller at 5.8 and 8.0 μm. Another noise contributor is source confusion, discussed by Dole et al. (2003). For aperture photometry in an aperture of area A

---

[6] See http://www.cfa.harvard.edu/irac/egs/.

TABLE 1
Aperture Corrections for Extended Groth Strip IRAC Mosaics

	Aperture Radius					
Band	2.5 pixels (1.53″)	3.5 pixels (2.14″)	5.0 pixels (3.06″)	2.45 pixels (1.5″)	3.3 pixels (2.0″)	4.9 pixels (3.0″)
3.6...............	-0.61 ± 0.05	-0.31 ± 0.03	-0.16 ± 0.03	-0.63 ± 0.05	-0.35 ± 0.04	-0.16 ± 0.03
4.5...............	-0.62 ± 0.04	-0.33 ± 0.03	-0.15 ± 0.03	-0.62 ± 0.04	-0.37 ± 0.04	-0.16 ± 0.03
5.8...............	-0.83 ± 0.04	-0.49 ± 0.04	-0.23 ± 0.03	-0.83 ± 0.04	-0.54 ± 0.04	-0.24 ± 0.03
8.0...............	-0.95 ± 0.02	-0.62 ± 0.02	-0.37 ± 0.02	-0.95 ± 0.02	-0.66 ± 0.02	-0.38 ± 0.02

Note.—Corrections to be added to aperture magnitudes to convert them to total magnitudes.
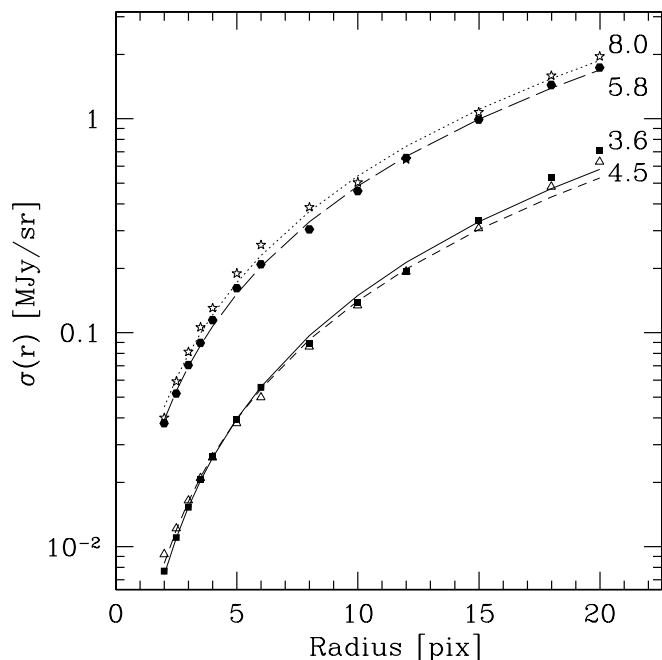
FIG. 3.—Standard deviations for sums of image counts (in MJy sr^{-1}) measured in empty regions on IRAC EGS mosaics. Counts were measured in circular apertures of radius r pixels. Lines represent fits of eq. (2) to the data. Solid line is for 3.6 μm (*squares*); short-dashed line for 4.5 μm (*triangles*); long-dashed line for 5.8 μm (*hexagons*); dotted line for 8.0 μm (*stars*).

TABLE 2
BACKGROUND NOISE FITS FOR IRAC MOSAICS

Band	a	b	σ_1
3.6.........................	0.54	0.85	1.66×10^{-3}
4.5.........................	0.92	0.66	1.87×10^{-3}
5.8.........................	2.19	0.59	6.65×10^{-3}
8.0.........................	1.96	0.71	6.31×10^{-3}

NOTE.—Fits are to eq. (2), with terms defined in § 2.

large compared to the point spread function, their equation (5) becomes

$$\sigma^2 = A(1.09/3600^2)BS_{\lim}^2(\gamma + 2)^{-1}, \qquad (1)$$

where the source density is represented by a power law, $dN/dS = B(S/S_{\lim})^{\gamma}$ sources deg^{-2} mag^{-1}. Based on the source counts given in § 4.1, source confusion noise is comparable to photon noise at 3.6 and 4.5 μm and smaller than photon noise at 5.8 and 8.0 μm. The present mosaics have an additional noise source because of the method of data taking. Observations in each location in the strip were taken at about the same time. Therefore, any temporal drift in the IRAC zero point translates nearly directly into a zero-point shift with spatial position on the scale of the IRAC field of view (5′). Errors in the flat field (gain matrix) will have a similar scale size, but will only affect bright sources.

In view of the difficulty of knowing all the noise sources, we have adopted an empirical approach to determining the noise. Aperture photometry of a set of 300 locations, distributed over the field and free of visible sources, gave a measure of variance for a range of aperture sizes at each wavelength. The variance for aperture sizes up to 12 pixels radius fits a function of the form suggested by Labbé et al. (2003),

$$\sigma(r) = \sigma_1 r (a + br), \qquad (2)$$

where σ_1 is the pixel-to-pixel rms noise and r is the aperture radius. The data and fits are shown in Figure 3; Table 2 gives the coefficients σ_1, a, and b. The first term corresponds to the combined effects of source confusion and Poisson noise, and the second term corresponds to the zero-point uncertainty at any location. It is dominant for extended sources and amounts to 0.02 MJy sr^{-1} at the two shorter wavelengths and 0.05 MJy sr^{-1}

at the two longer wavelengths. This noise could potentially be decreased by different reduction techniques that force the mosaic zero point to be constant (e.g., Fixsen et al. 2000). For a radius of 3 pixels (=1.8″), about the smallest aperture feasible, the first term implies noise of 0.04, 0.05, 0.5, and 0.4 μJy in the four IRAC bands, respectively. For the two longer channels, this is roughly consistent with source confusion noise and represents the approximate limit to which an optimum technique could extract point sources. For the shorter two wavelengths, the empirical "linear" noise is much smaller than the estimated confusion noise. The reason is unclear, but the most likely explanation is that the zero-point uncertainty is so large as to make it impossible to measure the empirical confusion noise. The total empirical noise $\sigma(r)$ in a small beam is consistent with expected source confusion noise.

3. SOURCE IDENTIFICATION AND PHOTOMETRY

To construct catalogs from the IRAC EGS mosaics, we used the SExtractor package (v 2.5.0; Bertin & Arnouts 1996) as is becoming standard in the field. We experimented with the input parameters to achieve an acceptable balance between completeness and reliability (as judged by eye, but see also § 3.1). The 3.6 and 4.5 μm mosaics are quite similar to each other in degree of crowding and background level, as are the 5.8 and 8.0 μm mosaics, but the short and long wavelength pairs are quite different from each other, so we derived 2 sets of input parameters for the two wavelengths regimes. The key values are given in Table 3. Most parameter settings were close to the defaults. The largest differences were the choice not to filter the images prior to detection and setting the deblending minimum contrast parameter to zero for the 3.6 and 4.5 μm images: these helped to improve the deblending of crowded sources, particularly at the shorter wavelengths.

The coverage images generated during mosaicking were used in two different ways as SExtractor input. In a fairly standard procedure, the coverage maps were used as "weight maps" for detection, such that a faint object appearing on a deeper area of the image receives greater weight than one near the crust. We also generated a "flag" image by combining the individual band mosaics' coverage maps with a minimum function and setting areas near bright stars affected by muxbleed or pulldown to have flag values of 1. By including the flag values in the SExtractor output, sources in regions of low coverage or near image artifacts could be easily eliminated from the final catalog. Mosaic regions with coverage >10 images (40 images at 8.0 μm) in all bands, a total area of about 1362 arcmin^2 (0.38 deg^2), were used to generate the catalog. The area within the EGS lost to artifact masking is about 15 arcmin^2, half of this in a 7.8 arcmin^2 region around and between the two brightest stars, centered on J2000.0 coordinates 14^{h}23^{m}11.5^s, 53°34′02″.

SExtractor was used to measure source magnitudes in a number of different ways. The first method is standard circular aperture

TABLE 3
Parameter Settings for SExtractor

Parameter	3.6/4.5	5.8/8.0
DETECT_MINAREA (pixels)	5	5
DETECT_THRESH	1.5	3
FILTER...	N	N
DEBLEND_NTHRESH..........................	64	64
DEBLEND_MINCONT.........................	0	0.005
SEEING_FWHM (arcsec).....................	1.8	2.0
GAIN..	$3, 2.65 \times 10^5$	$6.28, 18.5 \times 10^4$
BACK_SIZE (pixels).........................	200	200
BACK_FILTERSIZE...........................	3	3
BACKPHOTO_TYPE............................	LOCAL	LOCAL
BACKPHOTO_THICK..........................	24	24
WEIGHT_TYPE	MAP_WEIGHT	MAP_WEIGHT

photometry, in apertures of radius 2.5, 3.5 and 5.0 pixels (1.53″, 2.14″, and 3.06″).[7] These magnitudes were corrected to total magnitudes using point-source corrections derived from the mosaic PSF images and given in Table 1. Also recorded were SExtractor's AUTO and ISOCOR magnitudes, which measure the total flux within the Kron radius and the isophotal area above the background (with a correction for flux in the PSF wings), respectively. The isophotes used for photometry were determined separately for each channel; they correspond to the level of the detection thresholds above the background (given in Table 3). No additional aperture corrections beyond those performed by SExtractor were applied to the AUTO and ISOCOR magnitudes. We did not attempt to measure magnitudes by PSF-fitting. Analysis of very deep observations in the "IRAC Dark field" (J. Surace 2007, private communication) showed that most faint IRAC sources are slightly resolved; for these objects, aperture photometry is more accurate.

To compute photometric uncertainties, SExtractor assumes that the background sky noise is Poisson and uncorrelated between

---

[7] In apertures of this size, a significant fraction of the flux comes from pixels only partially within the aperture. To test that, SExtractor correctly deals with these "partial pixels" we used it to perform aperture photometry on an image with a uniform background. There were small systematic differences between the total flux in small apertures and the expected values, but the differences were <1%, with no dependence on the aperture position relative to the pixel center.

adjacent pixels. This is not the case for our resampled, mosaicked data, so we followed Gawiser et al. (2006) in deriving a correction to the uncertainties, based on our noise measurements in § 2. To correct the SExtractor flux uncertainties we apply

$$\frac{\sigma_{\text{phot, corr}}}{\sigma_{\text{phot, SE}}} = \left[\frac{\sigma^2(r) + F/G}{\sigma_1^2 \pi r^2 + F/G} \right]^{1/2}, \qquad (3)$$

where F is the object flux as measured in MJy sr^{-1} units, G is the effective gain (electrons per image unit, see Table 3), and $\sigma^2(r)$ is computed from equation (2) with the coefficients for each band given in Table 2. The radius r is the measurement aperture for aperture magnitudes, the Kron radius in pixels for AUTO magnitudes, and (ISOAREA/π)$^{1/2}$ for isophotal magnitudes. The magnitude of the correction factor varies with aperture size and, for objects in the number count peak, is typically about a factor of 2 for ISOCOR and aperture magnitudes and 4 for AUTO magnitudes, which use larger apertures.

Aperture magnitudes are of course most appropriate for point sources, and some sources in the IRAC EGS mosaics are clearly resolved. Most of the obvious extended sources in the EGS data are bright nearby galaxies which can be identified with the SExtractor CLASS_STAR output parameter. The distribution of CLASS_STAR as a function of magnitude, combined with visual inspection of the images, shows that accurate separation between resolved and unresolved objects is possible for the 5785 sources brighter than [3.6]$_{\text{AB, auto}}$ = 20.25. Brighter than this limit, 3224 sources (56%) have CLASS_STAR < 0.05 and are therefore likely to be extended. Comparison of the corrected aperture magnitudes to AUTO and ISOCOR values for these sources suggests that, as expected, the two smaller aperture magnitudes underestimate the total flux, by 10%–20% on average. The 5 pixel–radius aperture magnitudes are within about 5% of the AUTO and ISOCOR measurements, as are all of the corrected aperture magnitudes for point sources in the same magnitude range. Most of the extended sources are relatively small, $r < 10″$. However, 13 objects are large enough ($r_{\text{iso}} = [A_{\text{iso}}/\pi]^{1/2} > 12″$ as measured on the 3.6 μm image) to require the use of the "extended source calibration."[8] Table 4 gives the correction factors for each object, derived using the measured r_{Kron}

---

[8] See http://ssc.spitzer.caltech.edu/irac/calib/extcal/index.html.

TABLE 4
Photometry Corrections for Individual Extended Sources

EGSIRAC	AUTO Magnitudes				ISO Magnitudes			
	[3.6]	[4.5]	[5.8]	[8.0]	[3.6]	[4.5]	[5.8]	[8.0]
EGSIRAC J141503.63+520434.1	0.07	0.03	0.15	0.23	0.07	0.03	0.10	0.17
EGSIRAC J141503.93+520909.6	0.07	0.04	0.16	0.25	0.07	0.02	0.11	0.24
EGSIRAC J141545.95+521328.0	0.05	0.01	0.09	0.20	0.06	0.02	0.07	0.21
EGSIRAC J141600.38+520617.5	0.08	0.04	0.19	0.26	0.06	0.02	0.10	0.20
EGSIRAC J141607.60+520810.7	0.06	0.02	0.09	0.17	0.06	0.02	0.06	0.11
EGSIRAC J141612.11+520936.8	0.06	0.02	0.14	0.21	0.06	0.02	0.08	0.18
EGSIRAC J141747.26+524102.8	0.07	0.02	0.13	0.21	0.06	0.01	0.05	0.20
EGSIRAC J141807.07+524150.1	0.07	0.03	0.13	0.19	0.06	0.02	0.09	0.18
EGSIRAC J141910.27+525151.1	0.05	0.01	0.11	0.23	0.06	0.02	0.08	0.20
EGSIRAC J142012.48+530729.7	0.06	0.02	0.12	0.22	0.06	0.02	0.06	0.21
EGSIRAC J142054.17+530705.7	0.07	0.03	0.19	0.25	0.07	0.03	0.15	0.20
EGSIRAC J142149.83+532005.2	0.05	0.01	0.07	0.14	0.06	0.02	0.04	0.08
EGSIRAC J142156.23+532601.7	0.05	0.01	0.07	0.16	0.06	0.01	0.03	0.13

Notes.—Corrections are in magnitudes to be added to the AUTO and ISOCOR magnitudes, and have already been applied to the magnitudes in Table 6. Values are derived from extended source correction formula at http://ssc.spitzer.caltech.edu/irac/calib/extcal/index.html.
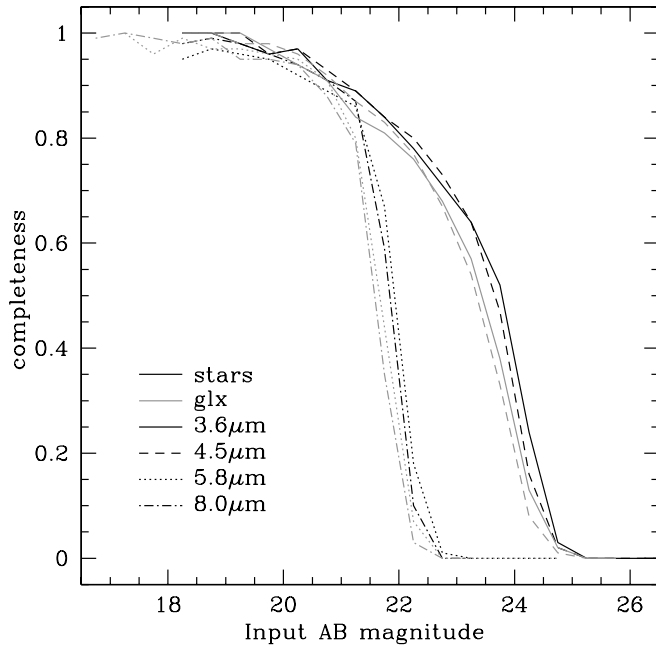
FIG. 4.—Completeness (fraction of artificial objects recovered) as a function of input magnitude for IRAC observations of the EGS. Black lines represent point sources and gray lines extended sources, with solid, long-dashed, short-dashed, and dot-dashed lines representing the 3.6, 4.5, 5.8, and 8.0 μm bands.

or $r_{\rm iso}$ in each band. These corrections *have* been applied to the final catalog.

3.1. *Completeness and Reliability*

Understanding the completeness and bias of a large survey is important for deriving its overall statistical properties, and the standard "artificial object" method was used to do this for the IRAC EGS catalogs. Both point and extended sources were generated using the ARTDATA package in IRAF with the mosaic point-spread functions (PSFs). There are a large number of possible parameters for artificial "galaxies" made with ARTDATA; we chose to use half "exponential disk" and half "de Vaucouleurs" profiles, with axial ratios >0.5 and effective radii $r_e = 1$ pixel.

Although this is a rather small size, after being convolved with the PSF, the resulting sources had similar sizes to the real objects in the images. The artificial sources were inserted into the mosaic images, then identified and photometered using SExtractor in the same manner as real sources. A total of 50,000 artificial sources were inserted with power-law ($\alpha = 0.3$) distributions of magnitudes in ranges $18 < [3.6, 4.5]_{\rm AB} < 26$, $17 < [5.8]_{\rm AB} < 25$, and $16.5 < [8.0]_{\rm AB} < 23.5$. The artificial sources were inserted 1500 at a time in the 5.8 and 8.0 μm mosaics, and 500 at a time in the more crowded 3.6 and 4.5 μm mosaics. An object was considered to be recovered if its position was within a radius of 1.5 pixels and its magnitude within 0.5 mag of an input artificial source. The second requirement reduces the chance that detection of a bright source will incorrectly be considered to be recovery of a nearby faint artificial source.

Completeness estimates were derived by sorting the artificial sources into bins by input magnitude and dividing the number of recovered sources by the number input. The results are shown in Figure 4 and given in tabular form in Table 5. The completeness curves for the 3.6 and 4.5 μm bands have a somewhat shallower falloff than those for the 5.8 and 8.0 μm bands. This is likely due to the effects of crowding: some sources which are well above the noise limit are not recovered because they fall too close to another source. As expected, the completeness for extended sources is somewhat lower than that for point sources. The 50% point-source completeness limits in the 4 IRAC bands are $m_{\rm AB} = 23.8, 23.7, 21.9, 21.8$, or 1.1, 1.2, 6.3, and 6.9 μJy. The 50% completeness limits for extended sources are 0.3 mag brighter, corresponding to 1.5, 1.6, 8.3, and 9.1 μJy.

The artificial source tests also permit tests of SExtractor's photometry. Figures 5 and 6 show the results of sorting artificial objects into bins by input magnitude and computing the median offsets between input and recovered magnitudes. The aperture corrections described in § 2 were applied to the recovered aperture magnitudes. In general, the recovered magnitudes are fainter than the input magnitudes, but most offsets are consistent with zero within the scatter. As expected, the small-aperture magnitudes underestimate the total fluxes of extended sources, but large-aperture magnitudes (and to a lesser extent the isophotal and Kron magnitudes) recover the input flux, consistent

TABLE 5
Completeness Estimates for IRAC EGS Catalog

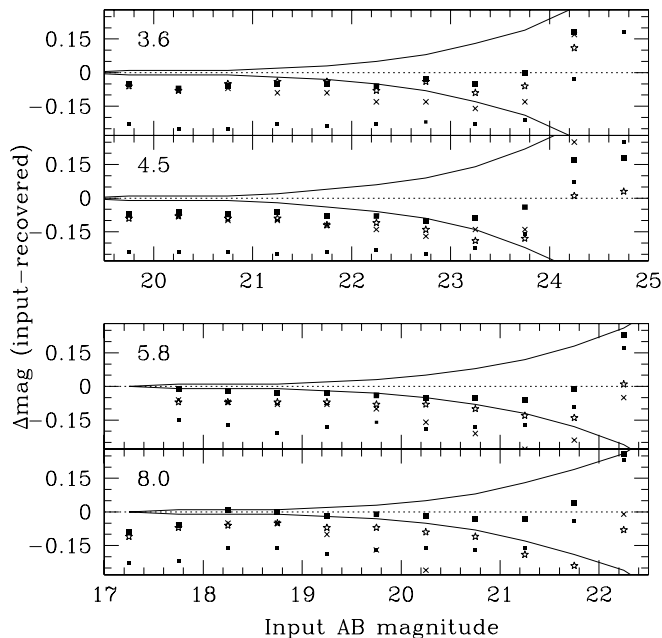| AB Magnitude	Point Source				Extended Source			
	[3.6]	[4.5]	[5.8]	[8.0]	[3.6]	[4.5]	[5.8]	[8.0]
17.25	...	...	...	...	...	...	1.00	1.00
17.75	...	...	...	...	...	...	0.96	0.99
18.25	1.00	1.00	0.95	0.98	1.00	1.00	0.99	0.98
18.75	1.00	1.00	0.97	0.99	1.00	1.00	0.97	0.99
19.25	0.98	1.00	0.96	0.98	1.00	0.98	0.97	0.95
19.75	0.96	0.96	0.95	0.96	0.97	0.98	0.96	0.95
20.25	0.97	0.97	0.92	0.94	0.94	0.96	0.95	0.94
20.75	0.91	0.93	0.89	0.91	0.91	0.92	0.91	0.88
21.25	0.89	0.89	0.86	0.87	0.84	0.87	0.80	0.79
21.75	0.84	0.84	0.67	0.59	0.81	0.83	0.44	0.35
22.25	0.78	0.80	0.18	0.10	0.76	0.77	0.07	0.03
22.75	0.71	0.73	0.01	0.00	0.68	0.67	0.00	0.00
23.25	0.64	0.64	0.00	0.00	0.57	0.54	0.00	0.00
23.75	0.52	0.47	0.00	...	0.38	0.33	0.00	...
24.25	0.24	0.16	0.00	...	0.13	0.08	0.00	...
24.75	0.03	0.02	0.00	...	0.02	0.01	...	...
25.25	0.00	0.00	...	...	0.00	0.00	...	...
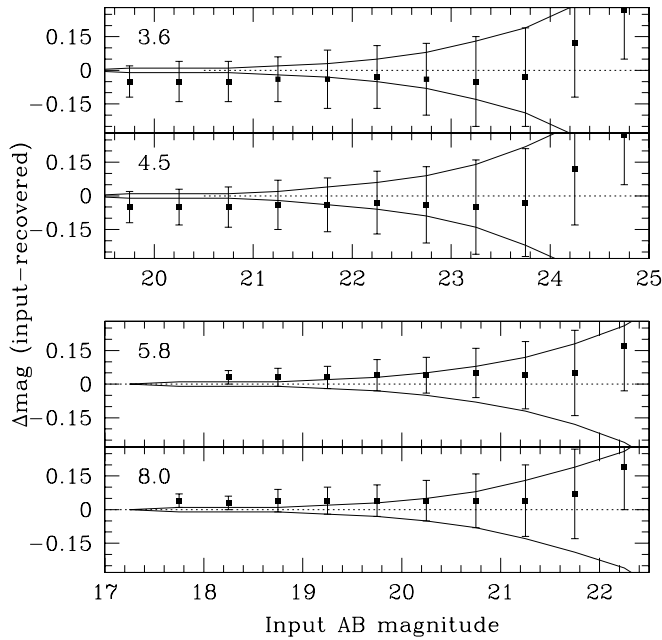
Fig. 5.—Difference between input and recovered magnitudes for artificial point sources in IRAC observations of the EGS. Recovered magnitudes are aperture magnitudes in 3.5 pixel radius apertures; vertical error bars are the standard deviations of the magnitude offsets in each bin. Solid lines connect the median magnitude uncertainties (for 3.5 pixel radius apertures) computed for the catalog objects in the same magnitude bins.
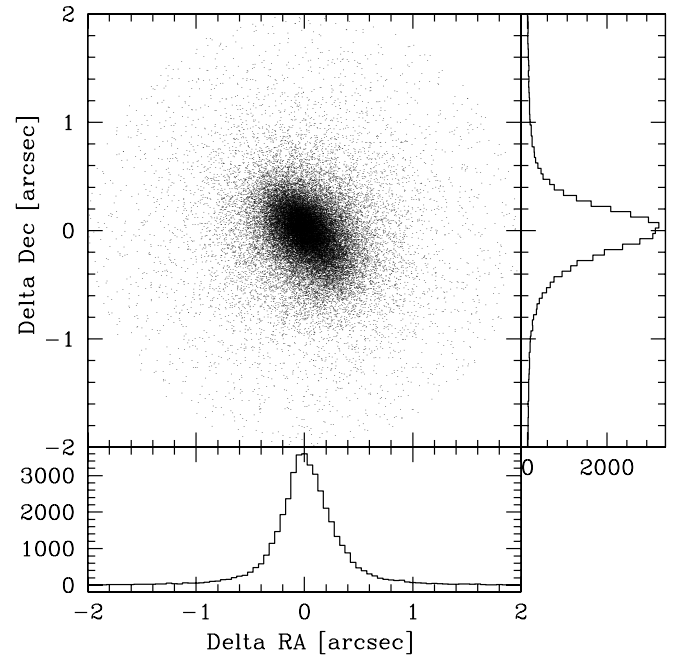

Fig. 7.—Astrometric offsets between IRAC source positions and those of sources in the DEEP2 photometric catalog, matched with a positional tolerance of 2.0″.

with the results in § 3. For point sources, the standard deviations of the magnitude offsets per bin range from about 0.01 mag for the brightest artificial sources measured with the smallest aperture to ~0.5 mag for the faintest artificial sources measured with MAG_AUTO. These values are roughly comparable to the median photometric uncertainties measured for the catalog objects in the same bins (shown in Fig. 5 as solid lines). For extended sources the bin standard deviations range from 0.08–0.6. For both point

and extended sources, the scatter between input and recovered magnitudes increases going from aperture magnitudes through MAG_ISOCOR and finally to MAG_AUTO. While these latter two magnitudes should provide better estimates of total flux for well-resolved sources, there are relatively few such objects in the EGS images, and we recommend the use of aperture magnitudes for most analyses of the catalog. In the analysis which follows in § 4 we use magnitudes measured in the 3.5 pixel (2.1″) radius aperture; this is near the "ideal" aperture chosen by Surace et al. (2005) and a reasonable compromise between the reduced contamination afforded by a smaller aperture and the greater flux fraction of a larger one.

To estimate the reliability of the catalog, we used the standard method of searching for sources on a negative image. This relies on the assumption that the noise is symmetric with respect to the background. Using the same SExtractor parameters described in § 3, 640 sources were detected on the 3.6 μm image in the (coverage > 10) region used to generate the catalog. The probability of spurious sources being detected at the same position in more than one band is proportional to the source density multiplied by the image and matching disk areas and is ≲10^{-4} for the source density found in the 3.6 μm negative image. Negative versions of the 4.5, 5.8, and 8.0 μm mosaics were created and analyzed in the same method as for the final catalog (by association with a source in the negative 3.6 μm image; see § 3.3). No matched sources were found in the longer wavelength negative mosaics at the same significance levels used for the real catalogs. Therefore, the only possible spurious sources are those detected only at 3.6 μm. There are about 9400 such sources, with an estimated spurious fraction of 640/9400 = 6.8%. This gives an overall spurious fraction for the full 3.6 μm selected catalog of 1.1%, or a reliability of 99%.

3.2. Astrometry

The precision and accuracy of positional measurements is an important quality in a large astronomical catalog. The quality of the astrometry in the IRAC mosaics is determined by both the
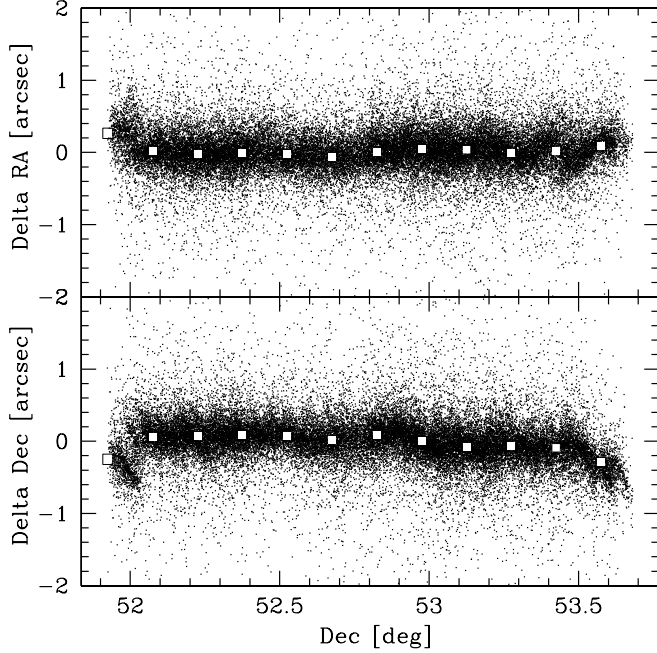

Fig. 6.—Difference between input and recovered magnitudes for artificial extended sources in IRAC observations of the EGS. Symbols are *stars*: MAG_AUTO; *crosses*: MAG_ISOCOR; *squares*: corrected aperture magnitudes in 2.5 pixel radius (*small*) or 5 pixel radius (*large*) aperture. Solid lines are the same as in Fig. 5.

Fig. 8.—Astrometric offsets between IRAC and DEEP2 sources, as a function of position. Squares are median values in 0.1° bins.

world coordinate systems for the individual BCD images and the accuracy with which they are combined. To assess the astrometric quality of the IRAC catalog, we matched 3.6 μm sources within a $2.0''$ radius to optical sources from the DEEP2 photometric catalog (Coil et al. 2004), which is tied to the SDSS coordinate frame. Figures 7 and 8 show the results. The accuracy of the IRAC astrometry is very high overall; the median offset is $0.012''$ ($-0.004''$) in R.A. (declination). The precision, as indicated by the standard deviations of the offsets (both $0.37''$), is consistent with expectations from the size of the IRAC PSF and pixels. There are larger offsets in both R.A. and decl. at the northern and southern ends of the EGS; these correspond to regions where the IRAC data were taken at only one epoch (see § 2). Evidently averaging two array position angles along the center of the EGS improved small errors in astrometry. To maintain consistency between the catalog and released mosaic images, we have not adjusted the positions of sources in the regions near the ends of the strip to make the median offsets equal to zero (they are still consistent with zero within our quoted precision). Catalog users wishing to adjust the astrometry for these sources should add ($0.2''$, $-0.2''$) to the coordinates of objects with $\delta < 52.025°$ and ($0.03''$, $-0.1''$) to the coordinates of objects with $\delta > 53.525°$.

3.3. Band Matching

The combination of measurements in the four IRAC bands was done using SExtractor's "association" mechanism; the 3.6 μm catalog was used as the master catalog, with sources in the other three bands associated by pixel position. We chose this method rather than "dual-image" mode (in which source and aperture positions are derived from a master image and used identically on other images), because there were small (<2 pixel or $1.2''$) but noticeable shifts between the mosaics in different bands, particularly at the ends of the EGS. The offset appears to be between the two IRAC fields-of-view (3.6/5.8 and 4.5/8.0), suggesting some relation to the mapping strategy used, although its exact cause is unclear. The offsets would have been problematic for dual-image mode, but the shifts were small enough that objects were matched between catalogs without difficulty. Re-

quiring a 3.6 μm detection does not unduly bias the catalog; less than a few hundred objects are detected at 4.5, 5.8 or 8.0 μm without a corresponding 3.6 μm detection. All of these objects are faint; many "8.0 μm – only objects" are in fact detections of the Galactic cirrus emission at the southeast end of the EGS, while others are the result of differences in deblending between different bands.

The IRAC EGS catalog is presented in Table 6.[9] This is a 3.6 μm selected catalog, so all objects are detected in this band. Objects undetected in the other bands have all parameters listed as zero. The aperture corrections given in Table 1 have been applied to all aperture magnitudes. As discussed in § 3, only the area of sky with exposure time >2000 s in all four IRAC bands was used to generate the catalog. Positions reported are as measured on the 3.6 μm image (see § 3.2 for discussion of astrometric accuracy). The magnitude uncertainties given are statistical and do not include the systematic calibration uncertainty (2%; Reach et al. 2005). Saturation limits are (see § 2) $m_{AB} = 15.7$, 15.7, 13.5, 13.5, or 2, 2, 14, and 14 mJy in the four IRAC bands. The columns of Table 6 are described in Table 7. The first seven columns are given only once per object, and the remaining columns once per band per object.

Because the 3.6 and 4.5 μm bands are more sensitive than the 5.8 and 8.0 μm bands, many sources are detected in only the two short-wavelength images. The 3.6 μm selected catalog contains 57,434 objects, with 48,066, 16,286, and 13,556 detected at 4.5, 5.8, and 8 μm (detection fractions of 84%, 28%, and 24%). While the 3.6 and 4.5 μm images have similar sensitivities, some of the faintest objects are too blue to be detected at 4.5 μm; objects at the 3.6 μm detection limit will only have a 4.5 μm detection if they have $[3.6] - [4.5] > -2.5 \log \left[f_{lim}(3.6)/f_{lim}(4.5) \right] \sim +0.1$. In the interests of releasing as complete a catalog as possible, we have included all SExtractor detections in Table 6. The signal-to-noise ratios of these detections, as measured by photometric uncertainty within the 3.5 pixel radius aperture, goes down to about S/N ~ 2. A less-complete but more-reliable catalog is also available through the Web site listed above, in which we have included only objects detected with S/N ≥ 5. This catalog reaches just below the 50% completeness levels and includes 44,772, 38,017, 13,486, and 11,546 sources in the four IRAC bands.

Confusion is significant in the two shorter wavelength images of the EGS. The number of beams per source, based on a beam area $\Omega = \pi \sigma^2$ ($\sigma = $ FWHM/2.35; Hogg 2001),[10] is about 28 at 3.6 μm, 35 at 4.5 μm, and $\sim$97 at 5.8 and 8.0 μm. Another measure of confusion is provided by matching IRAC sources with those from a catalog at higher resolution. Such a catalog is available from the *Hubble Space Telescope* Advanced Camera for Surveys (ACS) observations of the central $70.5' \times 10.1'$ of the EGS: there are about 8×10^4 ACS sources (to $I_{AB} = 28.1$) in this area and about 3.1×10^4 IRAC 3.6 μm sources. With a match radius of $2.0''$, about 93% of 3.6 μm sources were matched to an ACS source. The IRAC sources without ACS counterparts comprise two groups: stars which show diffraction spikes on the ACS image but are not included in the ACS catalog ($\sim$10%) and sources which are undetected on the optical image. About half of the ACS-undetected sources are relatively bright ($[3.6]_{AB} \lesssim 21$); these interesting sources will be followed up in a future contribution. About 30% of the matched IRAC sources had two or more ACS sources within $2.0''$ and roughly 7% had three or more

---

[9] Also available at http://www.cfa.harvard.edu/irac/egs/.
[10] Some authors use a definition of Ω which is twice as large, which reduces the number of beams per source by a factor of 2.

TABLE 6
Extended Groth Strip 3.6 μm selected Catalog

EGSIRAC	R.A. X_i	Decl. Y_i	Class A_i	Flags $r_{k,i}$	Cov a_i	$r_{1/2}$ b_i	θ_i	$m_{AU,i}$	$m_{ISO,i}$	$m_{AP,i}$	$\sigma(m_{AP,i})$
J141405.74+520024.2.........	213.523955	52.00674	0.212	0	11	1.774	...	...	...	...	...
	13140.84	1386.28	20	4.18	1.15	1.04	−56.21	23.12 ± 0.22	23.06 ± 0.15	22.82 22.86 22.98	0.12 0.18 0.34
	13141.13	1385.58	16	5.59	1.19	0.86	−60.09	23.25 ± 0.32	23.23 ± 0.16	22.94 22.97 23.12	0.15 0.21 0.37
	0.00	0.00	0	0.00	0.00	0.00	0.00	0.00 ± 0.00	0.00 ± 0.00	0.00 0.00 0.00	0.00 0.00 0.00
	0.00	0.00	0	0.00	0.00	0.00	0.00	0.00 ± 0.00	0.00 ± 0.00	0.00 0.00 0.00	0.00 0.00 0.00
J141406.12+520018.1.........	213.525528	52.005052	0.169	0	11	1.537	...	...	...	...	...
	13145.00	1375.56	11	5.20	1.04	0.96	74.63	23.96 ± 0.70	23.67 ± 0.21	23.50 23.60 23.93	0.24 0.36 0.84
	0.00	0.00	0	0.00	0.00	0.00	0.00	0.00 ± 0.00	0.00 ± 0.00	0.00 0.00 0.00	0.00 0.00 0.00
	0.00	0.00	0	0.00	0.00	0.00	0.00	0.00 ± 0.00	0.00 ± 0.00	0.00 0.00 0.00	0.00 0.00 0.00
	0.00	0.00	0	0.00	0.00	0.00	0.00	0.00 ± 0.00	0.00 ± 0.00	0.00 0.00 0.00	0.00 0.00 0.00
J141406.46+515947.4.........	213.526918	51.99651	0.012	3	11	2.268	...	...	...	...	...
	13180.00	1339.90	57	16.49	1.52	1.43	−30.59	22.33 ± 1.11	22.01 ± 0.17	22.48 22.42 22.32	0.09 0.12 0.12
	13181.47	1338.56	48	14.38	1.70	1.43	67.45	22.29 ± 0.83	22.12 ± 0.15	22.54 22.44 22.34	0.10 0.12 0.17
	0.00	0.00	0	0.00	0.00	0.00	0.00	0.00 ± 0.00	0.00 ± 0.00	0.00 0.00 0.00	0.00 0.00 0.00
	0.00	0.00	0	0.00	0.00	0.00	0.00	0.00 ± 0.00	0.00 ± 0.00	0.00 0.00 0.00	0.00 0.00 0.00

NOTE.—Table 6 is published in its entirety in the electronic edition of the *Astrophysical Journal Supplement*. A portion is shown here for guidance regarding its form and content.

TABLE 7

Column Descriptions for IRAC EGS Catalog

Column	Description	Units
ID	Format EGSIRAC Jhhmmss.ss + ddmmss.s	...
ALPHAWIN_J2000	Right ascension in epoch J2000.0[a]	Degrees
DELTAWIN_J2000	Declination in epoch J2000.0	Degrees
CLASS_STAR............................	SExtractor classification in 3.6 μm image, from 0 (nonstellar) to 1 (stellar)	...
FLAGS	SExtractor FLAGS in 3.6 μm image, range 0–3[b]	...
COVERAGE................................	Minimum coverage in four bands at object location[c]	...
FLUX_RADIUS..........................	Radius containing 50% of enclosed flux at 3.6 μm	Pixel
XWIN_IMAGE_i........................	Object barycenter in band i	Pixel
YWIN_IMAGE_i........................	Object barycenter	Pixel
ISOAREA_IMAGE_i	Isophotal area above detection threshold	Pixel
KRON_RADIUS_i	Kron radius	Pixel[d]
AWIN_IMAGE_i........................	Semimajor axis	Pixel
BWIN_IMAGE_i........................	Semiminor axis	Pixel
THETAWIN_J2000_i	Position angle, east of north	Degrees
MAG_AUTO_i............................	Kron magnitude	AB mag
MAGERR_AUTO_i	Kron magnitude uncertainty	AB mag
MAG_ISOCOR_i........................	Magnitude in isophote above detection threshold	AB mag
MAGERR_ISOCOR_i	Isophotal magnitude uncertainty	AB mag
MAG_APER_i............................	Aperture magnitudes in 2.5,3.5, and 5 pixel radii	AB mag
MAGERR_APER_i	Aperture magnitude uncertainties	AB mag

[a] SExtractor's "windowed" parameters for image location and shape (e.g., ALPHAWIN_IMAGE, AWIN_IMAGE) are used because the extensive comparison by Becker et al. (2008) showed that these were superior to the older "isophotal" measurements (e.g., ALPHA_J2000, A_IMAGE).
[b] FLAGS is the bitwise sum of values 1 (object has near neighbors or bad pixels) or 2 (object was originally blended with another one).
[c] Minimum was computed as min($C(3.6)$, $C(4.5)$, $C(5.8)$, $C(8.0)/4$), where $C(\lambda)$ is the number of frames combined in band λ at the object location.
[d] SExtractor outputs this parameter in units of semimajor axis; the value given here is multiplied by A_IMAGE to convert to pixels.
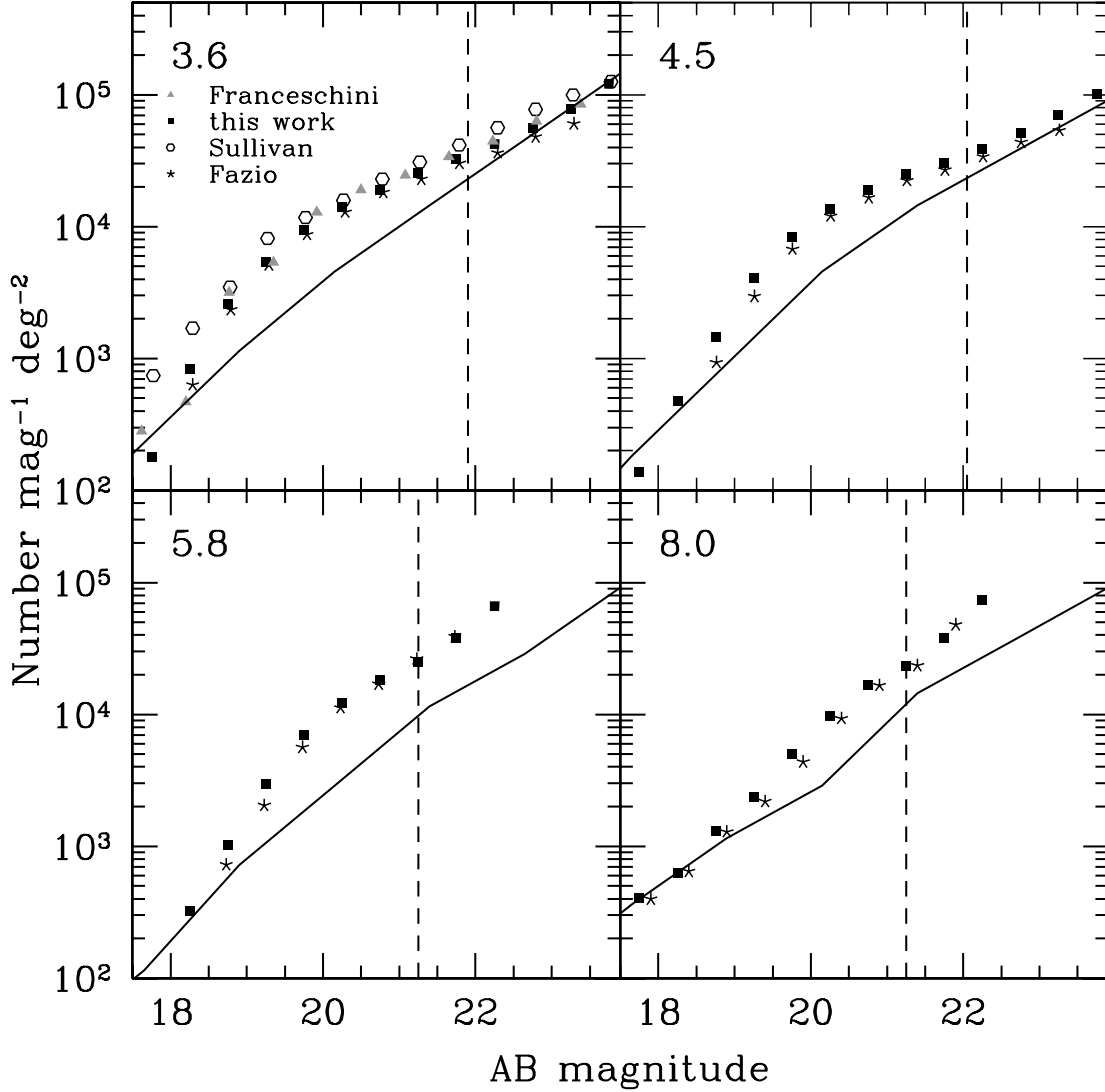
Fig. 9.—Differential number counts derived from IRAC surveys. *Squares*: This work (with model star counts subtracted); asterisks: EGS number counts from Fazio et al. (2004a); *circles*: number counts from Sullivan et al. (2007); *triangles*: number counts from Franceschini et al. (2006). *Solid lines*: Models (total counts) from Lacey et al. (2007). All counts are corrected for incompleteness; vertical dashed lines show the 80% completeness limit of the present IRAC EGS catalog.

ACS sources within this radius. Although SExtractor attempts to correct for flux from neighboring objects when doing photometry, up to one-third of IRAC sources may have their photometry affected at some level by confusion.

4. ANALYSIS

4.1. *Number Counts*

A fundamental property of any astronomical catalog is the distribution of sources as a function of flux. To compare our catalog with other recent work, we derived number counts of galaxies using the SExtractor aperture magnitudes in the 2.1″ radius aperture. The counts have been corrected for incompleteness using the results of § 3.1. The star count model for the EGS given in Fazio et al. (2004a) was subtracted from the raw number counts; no other attempt was made to separate stars and galaxies. Figure 9 shows the number counts derived from the EGS data and compares them to other recent measurements in the IRAC bands (Fazio et al. 2004a; Franceschini et al. 2006; Sullivan et al. 2007) and the models of Lacey et al. (2007). There is excellent

agreement with the results of Fazio et al. (2004a), as expected, since the data and analysis methods used are very similar. Our number counts are reasonably consistent with previous results, except at the faintest magnitudes where our incompleteness may be underestimated. The Lacey et al. (2007) models produce the correct general trends but are offset from the data by up to a factor of 2, a feature also apparent in their Figure 1. Lacey et al. (2007) did not consider this offset serious, since their models had not been tuned to match the *Spitzer* data.

4.2. *Color Distributions*

Galaxy colors in the IRAC bands are affected by a number of components: the Rayleigh-Jeans tail of emission from starlight, polyaromatic hydrocarbon (PAH) emission, the redshifted 1.6 μm stellar opacity minimum, and (often red power-law) emission from an AGN. Determining the dominant source of emission for IRAC sources is complicated by the lack of redshift information for many sources; IRAC's sensitivity allows it to detect galaxies in the "redshift desert" where optical spectroscopic redshifts are not easy to obtain. But a general picture of the IRAC source can be
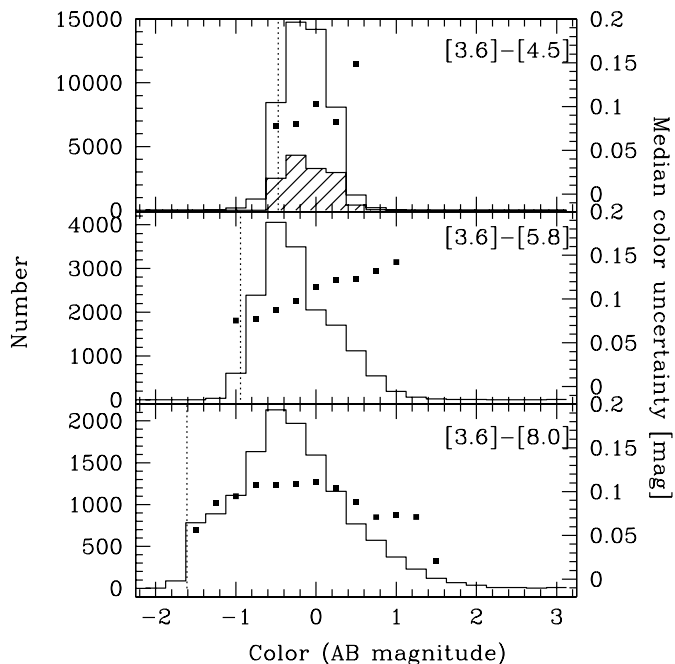
FIG. 10.—Distribution of IRAC colors for sources in the EGS catalog. The vertical lines denote the AB magnitude colors corresponding to Vega magnitudes of zero (the color expected for starlight). The hatched histogram in the top panel shows the distribution of [3.6] − [4.5] magnitudes for sources with an 8.0 μm detection. Squares indicate median color uncertainties in each color bin, according to the scale on the right side of the plot. All colors in this and following plots are based on corrected aperture magnitudes in a 3.5 pixel (2.1″) radius aperture.

FIG. 11.—IRAC color-magnitude diagrams [3.6] − [4.5] vs. [4.5], using aperture magnitudes measured in 2.1″ radius apertures. *Left*: 13,538 sources with an 8.0 μm detection. *Right*: 34,538 sources without an 8.0 μm detection. Horizontal error bars in the right panel indicate median color uncertainties in magnitude bins.

derived by examination of color distributions and comparison with models and other surveys. In the following analysis, all colors are measured using aperture magnitudes (including aperture corrections) in the aperture with radius 3.5 pixels (2.1″).

Figure 10 shows the distribution of IRAC source colors relative to the 3.6 μm band. As expected, few sources are bluer than unreddened stars, although PAH emission in the 3.6 μm band and CO absorption in the 4.5 μm band can cause some bluer colors. The [3.6] − [4.5] color distribution is relatively narrow and is similar for sources with and without 8.0 μm detections. The colors involving the two longer wavelength bands show much more dispersion, presumably because they depend on the variable strengths of the PAH features moving through the bands with redshift (see also Fig. 6 of Huang et al. 2007). Figure 11 shows a color-magnitude diagram for sources with and without 8.0 μm detections; the latter are simply fainter. The bright, blue objects in the left panel are stars; the red measured colors for the brightest objects are due to saturation in the 3.6 μm photometry.

The four IRAC bands can be combined in a number of ways to make two-color diagrams. Different authors plot these in different ways: as flux ratios, colors in the Vega system, and colors in the AB system. We have plotted all such diagrams in the AB system, which has the advantage that different combinations of colors can be easily compared, but the disadvantage of complicating comparisons to previous work. Figure 12 show two-color diagrams using the three possible combinations of all four IRAC bands. The three diagrams have some common features: a relatively tight distribution of sources with the bluest colors and two branches at redder colors. The blue sources are particularly well-separated in Figure 12c and are presumably dominated by stellar emission. In the models of Sajina et al. (2005) using the color
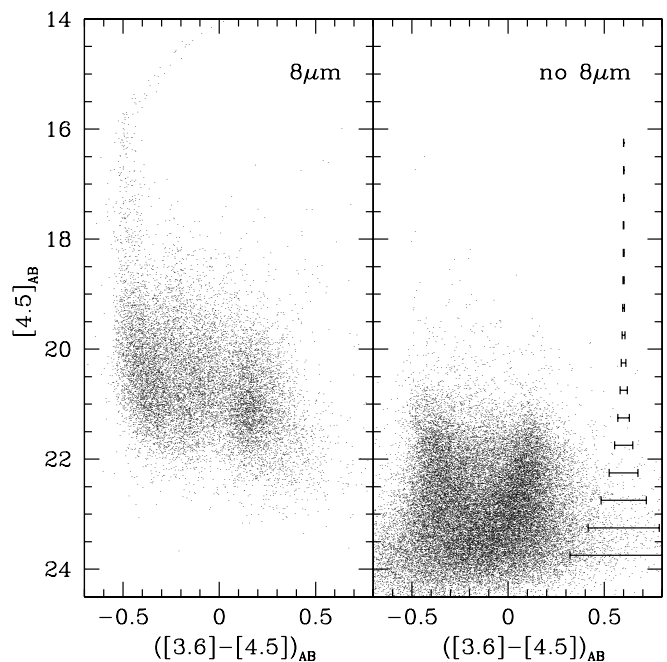
space of Figure 12b, the vertical branch is dominated by low-redshift galaxies with PAH emission, and the redder diagonal branch (which dominates the EGS distribution) is expected to be some mixture of AGN and high-redshift galaxies. Comparing Figure 12a to Figure 1 of Stern et al. (2005), the EGS catalog appears to contains fewer low-redshift, PAH-dominated galaxies (*top left*) but more sources in the "AGN wedge" (*middle right*), and the location expected for high-redshift normal galaxies (*bottom right*). This is consistent with the fainter flux limit of the EGS observations; these should contain more high-redshift galaxies than the IRAC Shallow Survey sources with optical spectroscopy plotted by Stern et al. (2005) and at $z \gtrsim 2$, star-forming galaxies begin to have similar observed colors to AGNs (Barmby et al. 2006). Similar conclusions can be drawn from comparison of Figure 12 with Figure 1a of Davoodi et al. (2006); as expected, the EGS has a lower proportion of low-redshift galaxies compared to the shallower but wider SWIRE survey.

There are many more combinations of three IRAC bands than can be conveniently plotted; Figure 13 shows a few. The color space shown in Figure 13a does not appear to be useful for separating different galaxy types; the sources all lie roughly along a single axis. Figure 13b is quite similar to Figure 12a, which might suggest that the 5.8 μm band does not provide much additional information over the combination of the other three bands. However, Figure 13c shows that the use of the three shortest bands works well to identify red sources. This color space was used by Figure 4 of Hatziminaoglou et al. (2005) to suggest a color criterion for type 1 AGN. However, Barmby et al. (2006) found that only about 30% of X-ray−selected AGNs in the EGS fell into their selection region. Figure 1c from Davoodi et al. (2006) suggest that objects red in both [3.6] − [4.5] and [4.5] − [5.8] are a mixture of AGNs and star-forming galaxies. The EGS contains a greater proportion of these objects than the SWIRE survey, as shown above. Figure 13d is the same color space plotted in Figure 1b of Davoodi et al. (2006); as seen there, the omission of the 3.6 μm
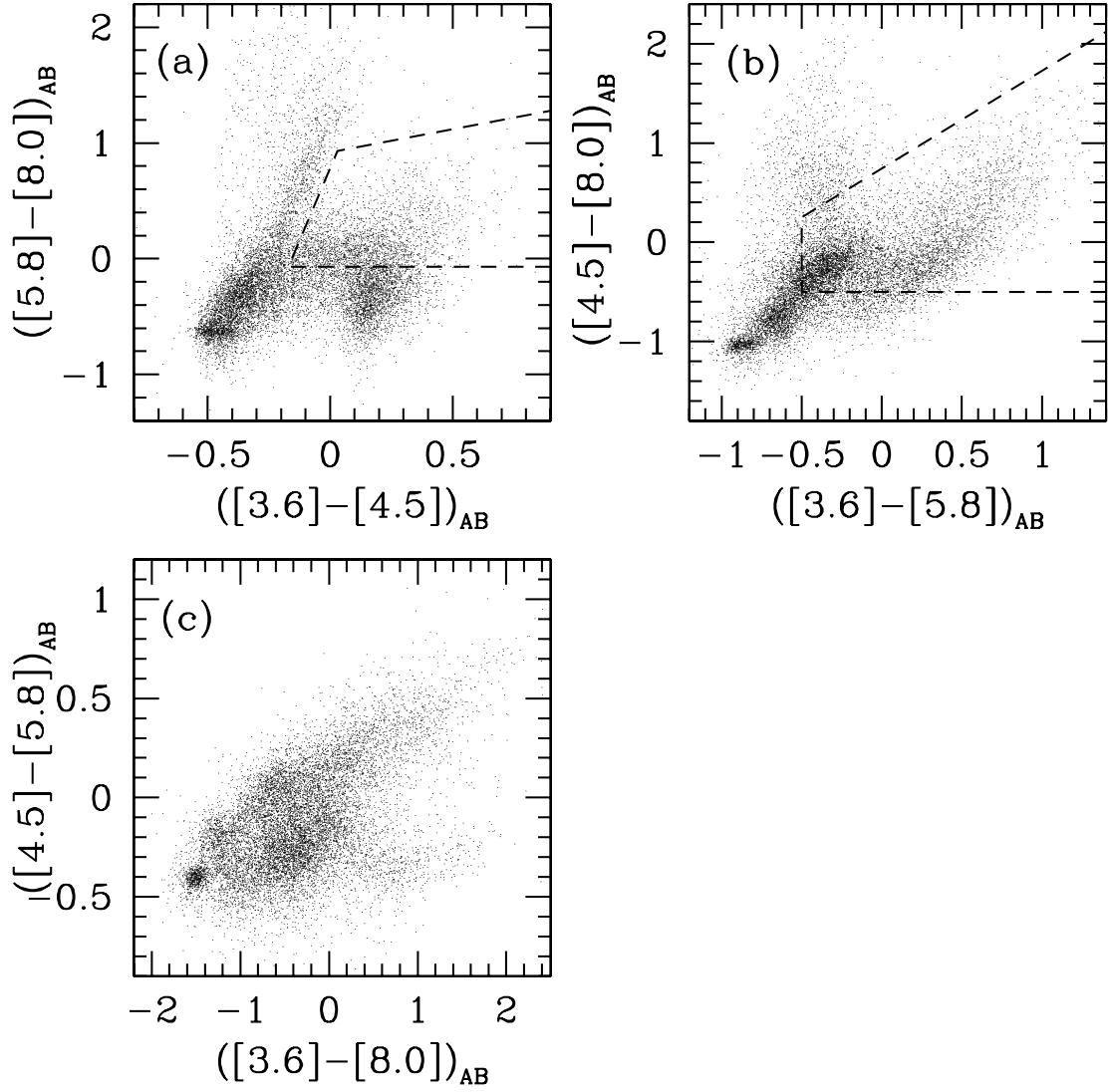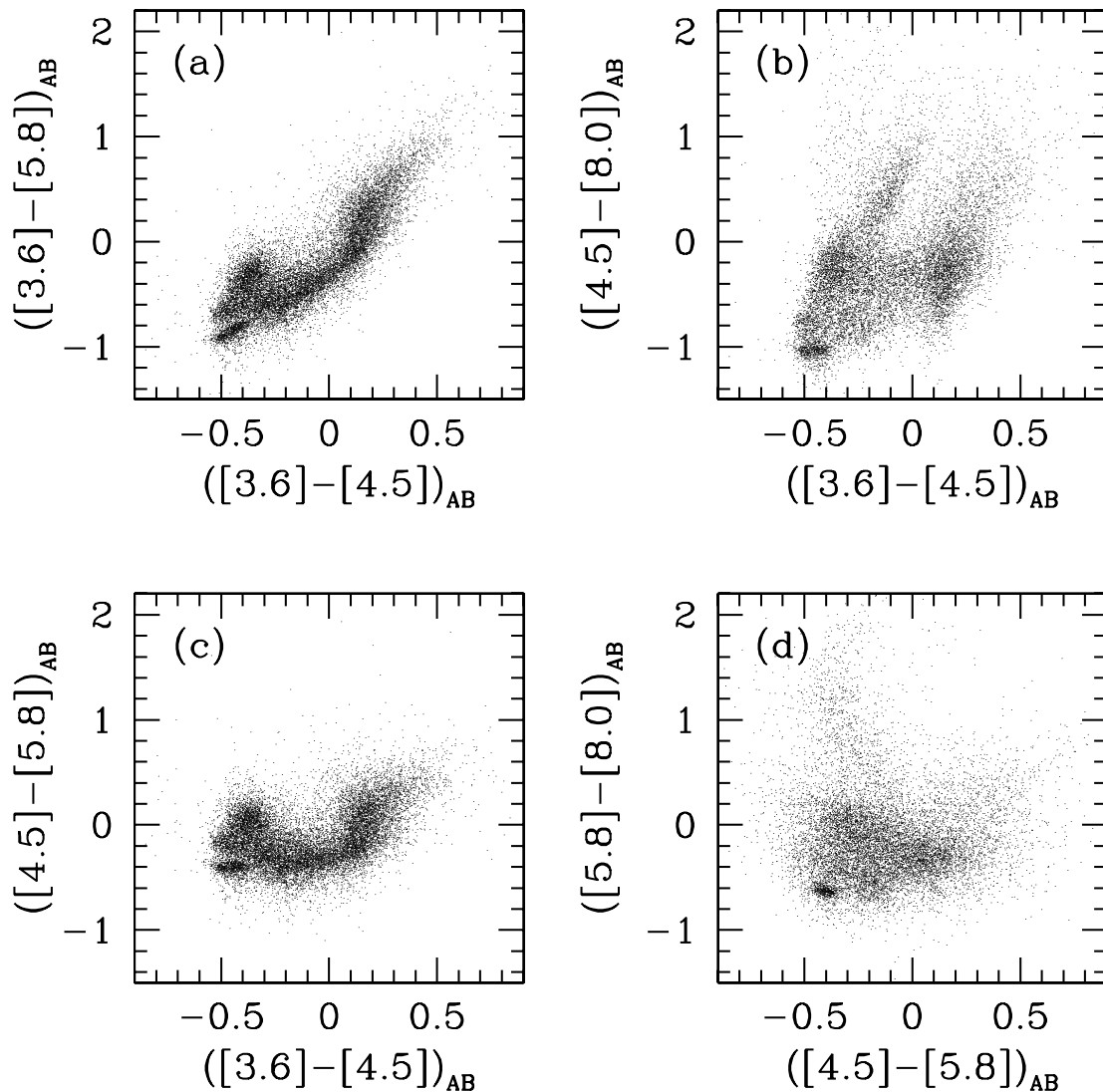
FIG. 12.—Two-color diagrams using four bands for sources in the EGS catalog, using aperture magnitudes measured in 2.1″ radius apertures. Only sources with four-band detections are plotted. Panel (*a*) corresponds to the color space used by Stern et al. (2005) and panel (*b*) to that used by Lacy et al. (2004) and Sajina et al. (2005); dashed lines show the outline of their "AGN wedges." The tight condensation of points at blue colors corresponds to galaxies dominated by stellar emission while the vertical or diagonal branches contain low-redshift galaxies and mixtures of high-redshift galaxies and AGN; see text for details.

Fig. 13.—Two-color diagrams using three bands for sources in the EGS catalog, using aperture magnitudes measured in 2.1″ radius apertures. Only sources with detections in all three relevant bands are plotted. See text for interpretation of color distributions.

band appears to decrease the separation between the various galaxy types.

5. SUMMARY

Observations of a 0.38 deg^2 area in the Extended Groth Strip using the Infrared Array Camera (IRAC) on the *Spitzer Space Telescope* detected tens of thousands of mid-infrared sources. The 3.6 μm selected catalog presented here includes 57,434 sources, of which most are detected at 4.5 μm and roughly one-quarter are detected at 5.8 and 8.0 μm. Number counts of sources are consistent with previous observations and marginally consistent with recent models. As expected, color distributions differ from those of shallower surveys by including a greater fraction of potential high-redshift sources. Future projects possible with this catalog include determination of photometric redshifts, galaxy stellar mass and luminosity functions, and mid-infrared characterization of populations such as luminous infrared galaxies and AGNs.

REFERENCES

Ashby, M. L. N., et al. 2006, ApJ, 644, 778
Barmby, P., et al. 2004, ApJS, 154, 97
Barmby, P., et al. 2006, ApJ, 642, 126
Becker, A. C., Silvestri, N. M., Owen, R. E., Ivezić, Z.& Lupton, R. H. 2008, PASP, 119, 1462
Bertin, E., & Arnouts, S. 1996, A&AS, 117, 393
Coil, A. L., Newman, J. A., Kaiser, N., Davis, M., Ma, C., Kocevski, D. D., & Koo, D. C. 2004, ApJ, 617, 765

Davis, M., et al. 2007, ApJ, 660, L1
Davoodi, P., et al. 2006, AJ, 132, 1818
Dole, H., Lagache, G., & Puget, J.-L. 2003, ApJ, 585, 617
Dye, S., et al. 2006, ApJ, 644, 769
Egami, E., et al. 2005, ApJ, 618, L5
Eisenhardt, P., et al. 2004, ApJS, 154, 48
Fazio, G. G., et al. 2004a, ApJS, 154, 39
———. 2004b, ApJS, 154, 10

Fixsen, D. J. Moseley, S. H., & Arendt, R. G. 2000, ApJS, 128, 651
Franceschini, A., et al. 2006, A&A, 453, 397
Gawiser, E., et al. 2006, ApJS, 162, 1
Hatziminaoglou, E., et al. 2005, AJ, 129, 1198
Hogg, D. W. 2001, AJ, 121, 1207
Huang, J.-S., et al. 2005, ApJ, 634, 137
———. 2007, ApJ, 664, 840
Labbé, I., et al. 2003, AJ, 125, 1107
Lacey, C. G., Baugh, C. M., Frenk, C. S., Silva, L., Granato, G. L., & Bressan, A. 2008, MNRAS, 385, 1155
Lacy, M., et al. 2004, ApJS, 154, 166
Le Floc'h, E., et al. 2005, ApJ, 632, 169
Papovich, C., et al. 2006, ApJ, 640, 92
Pérez-González, P. G., et al. 2005, ApJ, 630, 82
———. 2008, ApJ, 675, 234

Reach, W., et al. 2006, Infrared Array Camera Data Handbook, Version 3.0 (Spitzer Science Center)
Reach, W. T., et al. 2005, PASP, 117, 978
Rieke, G. H., et al. 2004, ApJS, 154, 25
Rigopoulou, D., et al. 2006, ApJ, 648, 81
Rowan-Robinson, M., et al. 2005, AJ, 129, 1183
Sajina, A., Lacy, M., & Scott, D. 2005, ApJ, 621, 256
Stern, D., et al. 2005, ApJ, 631, 163
Sullivan, I., et al. 2007, ApJ, 657, 37
Surace, J. A., et al. 2005, SWIRE Data Release 2 Documentation
Werner, M., et al. 2004, ApJS, 154, 1
Williams, R. E., et al. 1996, AJ, 112, 1335
Willner, S. P., et al. 2006, AJ, 132, 2159
York, D. G., et al. 2000, AJ, 120, 1579